PHOTONICS Research

Two-photon 3D printed spring-based Fabry–Pérot cavity resonator for acoustic wave detection and imaging

Heming Wei,[1] Zhangli Wu,[1] Kexuan Sun,[1] Haiyan Zhang,[1] Chen Wang,[2] Kemin Wang,[2] Tian Yang,[3] Fufei Pang,[1,*] Xiaobei Zhang,[1] Tingyun Wang,[1] and Sridhar Krishnaswamy[4,5]

[1]Key Laboratory of Specialty Fiber Optics and Optical Access Networks, Joint International Research Laboratory of Specialty Fiber Optics and Advanced Communication, Shanghai University, Shanghai 200444, China
[2]School of Mechatronic Engineering and Automation, Shanghai University, Shanghai 200444, China
[3]State Key Laboratory of Advanced Optical Communication Systems and Networks, Key Laboratory for Thin Film and Microfabrication of the Ministry of Education, School of Electronic Information and Electrical Engineering, Shanghai Jiao Tong University, Shanghai 200240, China
[4]Center for Smart Structures and Materials, Northwestern University, Evanston, Illinois 60208, USA
[5]e-mail: sridhar.krishnaswamy@northwestern.edu
*Corresponding author: ffpang@shu.edu.cn

Received 28 December 2022; revised 27 February 2023; accepted 28 February 2023; posted 2 March 2023 (Doc. ID 481858); published 28 April 2023

Optical fiber microresonators have attracted considerable interest for acoustic detection because of their compact size and high optical quality. Here, we have proposed, designed, and fabricated a spring-based Fabry–Pérot cavity microresonator for highly sensitive acoustic detection. We observed two resonator vibration modes: one relating to the spring vibration state and the other determined by the point-clamped circular plate vibration mode. We found that the vibration modes can be coupled and optimized by changing the structure size. The proposed resonator is directly 3D printed on an optical fiber tip through two-photon polymerization and is used for acoustic detection and imaging. The experiments show that the device exhibits a high sensitivity and low noise equivalent acoustic signal level of 2.39 mPa/Hz$^{1/2}$ at 75 kHz that can detect weak acoustic waves, which can be used for underwater object imaging. The results demonstrate that the proposed work has great potential in acoustic detection and biomedical imaging applications.

https://doi.org/10.1364/PRJ.481858

1. INTRODUCTION

Acoustic wave-based sensing and imaging methods have been widely studied in various important applications such as biomedical imaging and underwater safety monitoring [1–3]. The key role in such applications is to develop acoustic/ultrasonic sensors exhibiting high sensitivity, broad bandwidth, and high frequency response. Typically, piezoelectric-based sensors and transducers are used because they can respond to high-frequency acoustic waves with ultrahigh sensitivity and relatively high bandwidth. However, electrical transmission from the sensing elements to the detection at high frequencies could be noisy, and fabrication could be problematic at a very high response frequency. In view of these limitations, there are alternatives based on optical sensors, especially fiber optic sensors such as fiber Bragg gratings (FBGs) [4,5], fiber Fabry–Pérot interferometers (FPIs) [6–8], fiber Michelson interferometers (MIs) [9,10], fiber Mach–Zehnder interferometers (MZIs) [11,12] and Sagnac interferometers (SIs) [13,14]. These options all offer attractive advantages, including immunity to electromagnetic interference and a compact size, which could be very interesting for acoustic sensing and imaging. Compared to other fiber-optic acoustic sensors, FPI microresonators can be miniaturized as a fiber probe by easy fabrication approaches and can exhibit high sensitivity [15–18]. The basic principle of FPI-based acoustic sensors is the vibration of the thin diaphragm that modulates the cavity spacing, and the elasto-optical effect that modulates the cavity refractive index. However, the stiffness of the silica could be a fundamental limitation for acoustic wave-induced strain sensing.

To overcome this issue, various methods ranging from functional materials to novel structures have been proposed and demonstrated for highly sensitive acoustic wave sensing. For diaphragm-based FP sensors, polymer-based functional materials with a high-elastic property have been used to design highly sensitive FP acoustic sensors [15,16]. To further increase the sensitivity, 2D materials have been proposed for highly sensitive acoustic sensing because the diaphragms can be extra thin

[17–19]. However, fabrication of such sensors is complicated and prone to variability from sensor to sensor. An alternative is to design flexible structures [20–22] such as corrugated structure microsprings, which show flexibility and low stiffness and can significantly enhance the sensitivity. To further improve this interaction, Yao *et al.* proposed a spirally suspended optomechanical microresonator that used a 3D microprinting technique based on digital light processing (DLP) [23]. Due to its resonance with low stiffness, the device has a sensitivity of 118.3 mV/Pa and a low noise equivalent acoustic pressure level of 0.328 μPa/$Hz^{1/2}$ in the audio frequency range, which could be useful for low-frequency microphone applications. Note that the current designs are mostly focused on either a sensitive diaphragm or resonant supports without considering the mode coupling between the parts, which can significantly affect the sensing performance.

In this work, we propose what we believe, to the best of our knowledge, is a novel optomechanical resonator for acoustic wave sensing and imaging. The device consists of one thin diaphragm connected to several springs that act as the supports, all of which are directly 3D printed on an optical fiber tip through two-photon polymerization. The resonant frequency is optimized to investigate the mode coupling between the plate and spring vibrations. Several high-order plate-domain vibration modes are found within the range from 0 to 3 MHz, which can be determined by the spring vibration mode or the point-clamped circular plate vibration mode. The experiments show that the device exhibits a high sensitivity that can detect weak acoustic waves.

2. MODEL DESIGN AND SIMULATION

Figure 1 shows the proposed FP cavity resonator, which consists of several springs as the supports. According to the mechanical vibration theory, the spring has a resonant frequency given by [24]

$$f_s = \frac{r}{8\pi(R-r)^2 N}\sqrt{\frac{E}{\rho(1+\nu)}}, \tag{1}$$

where r is the wire radius, R is the outer radius of the spring, N is the number of active coils, and E, ρ, ν are, respectively, Young's modulus, the density, and Poisson's ratio of the materials. Here, a photoresist (IP-Dip Nanoscribe GmbH and Co. KG, Eggenstein-Leopoldshafen, Germany) is used for simulation. Note that a spring with low stiffness can enhance the vibration amplitude of the device for acoustic wave pressure sensing (at low frequencies). Figure 1(a) shows the schematic diagram of the device where p is the pitch of the spring and $l = p \times N$ is the free length of the spring. For an FP cavity, a thin plate can be clamped by the springs as shown in Fig. 1(a). Based on the clamped circular vibration theory, the resonant modes are related to [25]

$$f_p \sim \frac{h}{r_p^2}\sqrt{\frac{E}{12\rho(1-\nu^2)}}, \tag{2}$$

where h and r_p are the thickness and radius of the plate. This shows that the FP cavity length will be modulated by the plate vibration. Figure 1(b) shows the proposed device model, which can be directly fabricated on an optical fiber tip through two-photon direct laser writing. The exact resonant modes of the combined structure (plate with the spring supports) can only be numerically evaluated using COMSOL Multiphysics software. In the case of underwater environments, a resonant frequency at 81.2 kHz (M1) is obtained, as shown in Fig. 1(c), where the springs have $r = 3$ μm, $R = 9$ μm, $p = 10$ μm, $N = 5$, and the plate has $r_p = 50$ μm, $h = 5$ μm, and the input acoustic wave pressure is 100 Pa. The device also has other high-order vibration modes determined by the coupling between the springs and the plate. Several high-order plate-domain vibration modes at 654.4 kHz (M2), at 819.5 kHz (M3), and 890.1 kHz (M4) are found within the range from 0 to 3 MHz. The 3 dB bandwidths of these modes are 0.29 kHz, 0.49 kHz, and 0.27 kHz, which correspond, respectively, to acoustic Q of 2256.9, 1672.4, and 3296.7. This coupling can be optimized by varying the parameters of the springs and plate to change the stiffness. Here, we simulate the frequency of springs and the circular plate separately when one is rigidly constrained as the parameters change, and then compare it with the first-order vibration mode of the device.

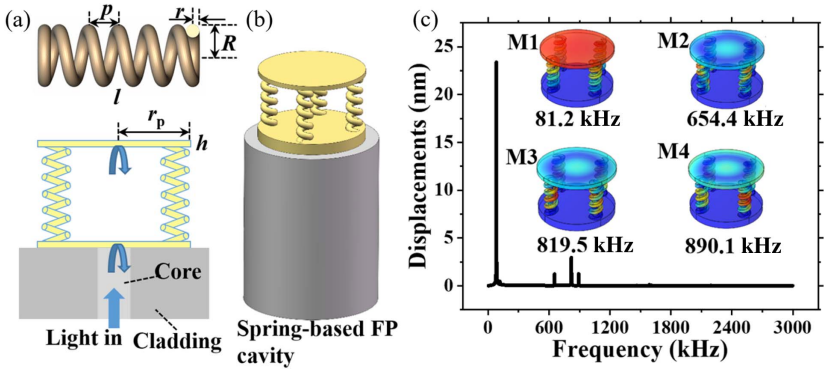

Fig. 1. Proposed spring-based FP optomechanical cavity resonator. (a) Schematic diagram of the spring resonator and the fiber-tip-based FP cavity where the springs are used as the supports with low stiffness. (b) Schematic diagram of the proposed FP cavity microresonator for acoustic wave detection and imaging. (c) Mode simulation of the proposed device used for acoustic wave sensing in a water environment. Four vibration modes are found within the range from 0 to 3 MHz when the parameters are initially set as $r = 3$ μm, $R = 9$ μm, $p = 10$ μm, $N = 5$, $r_p = 50$ μm, $h = 5$ μm: Mode 1 at 81.2 kHz (M1), Mode 2 at 654.4 kHz (M2), Mode 3 at 819.5 kHz (M3), and Mode 4 at 890.1 kHz (M4).

Figure 2 shows a simulation of the vibration modes of each part and the system. Here, the radius and thickness of the plate are set as 50 μm and 1 μm. It can be seen from Fig. 2(a) that the resonant frequency of the spring decreases while the resonant frequency of the plate increases as the outer radius increases. For the whole device, the frequency decreases due to the mode coupling between the springs and plate. Note that the stiffness will be high if the wire radius increases, and the resonant frequencies of the spring increase, while the frequency of the plate membrane slightly increases due to the increasing connections; hence, the resonant frequency of the whole device increases, as shown in Fig. 2(b). Note that the support conditions change as the outer radius and the wire radius change, which causes the resonant frequency of the plate membrane to also change.

In addition, the effect of the coil number and pitch was investigated. It was found that the frequency of the spring decreases as the coil number increases while the frequency of the plate membrane is almost unchanged. Therefore, the resonant frequency is then decreased, as shown in Fig. 2(c). The frequencies of the device do not change significantly when the pitch changes, as shown in Fig. 2(d). It is interesting to see that the frequency spectrum can be divided into three regions: a spring-dominated area, a plate-dominated area, and a maximal coupling area. Based on the frequency spectrum, each device with different domain-vibration modes can be designed for acoustic wave detection.

The stiffness of the springs does not change significantly as the plate thickness changes while the resonant frequency of the plate significantly increases as the thickness increases, as shown in Fig. 3. Figure 3(a) shows the frequency versus the thickness of the membrane when the outer radius, the wire radius, the pitch, and the coil number are, respectively, 9 μm, 3 μm, 10 μm, and 5. The three regions are still found when the membrane thickness changes, as shown in Fig. 3(b). As the frequency of the plate membrane is significantly larger than that of the spring, the resonant frequency of the device is almost unchanged, which is mainly determined by the springs.

3. FABRICATION AND CHARACTERIZATION

A. Fabrication

Based on the simulation results, the spring-dominant FP optomechanical cavity was designed and then fabricated using a direct laser writing technique through two-photon polymerization. First, a piece of single-mode fiber was cleaved and mounted by a fiber holder and immersed into a droplet of photoresist (IP-Dip, Nanoscribe), which was prepared on a 63× immersion objective. Here, the device was fabricated by a commercial two-photon 3D laser lithography system (Photonic Professional GT2, Nanoscribe) based on a femtosecond laser at 780 nm wavelength with 80 MHz repetition frequency. First, the beam was focused directly on the fiber tip. To increase the adhesion between the fiber and the printed device, the first writing layer was inside the fiber. Additionally, the power laser and writing speed were optimized to obtain structures with smooth surfaces [26,27].

First, two devices with different cavity lengths of 50 and 140 μm were printed. The springs have an outer radius of 9 μm, a wire radius of 3 μm, a coil number of 5, and a pitch of 10 μm, and the plate has a thickness of 5 μm and a radius of 50 μm. Figures 4(a) and 4(b) show scanning electron images

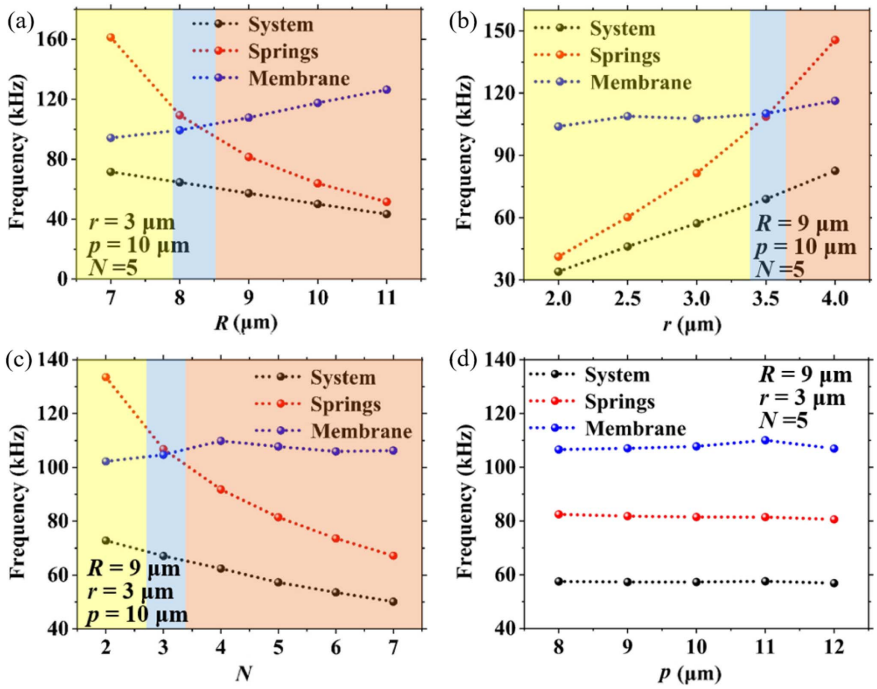

Fig. 2. Resonant frequency behavior of the whole device and its individual parts related to the parameters of (a) the outer radius, (b) the wire radius, (c) the coil number, and (d) the pitch. In these simulations, the resonant frequency of an individual part is studied assuming that the other part is rigidly constrained.

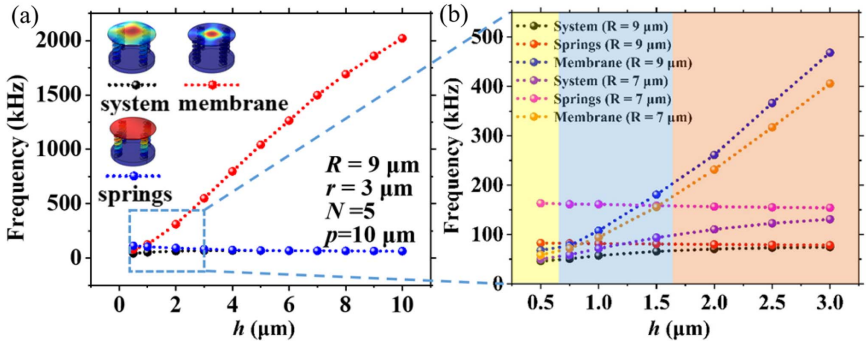

Fig. 3. Resonant frequency behavior of the device system and each part versus the plate membrane related to the parameters of the thickness within a range from (a) 0.5 to 10 μm and (b) 0.5 to 3 μm, where the outer radius is 9 μm and 7 μm.

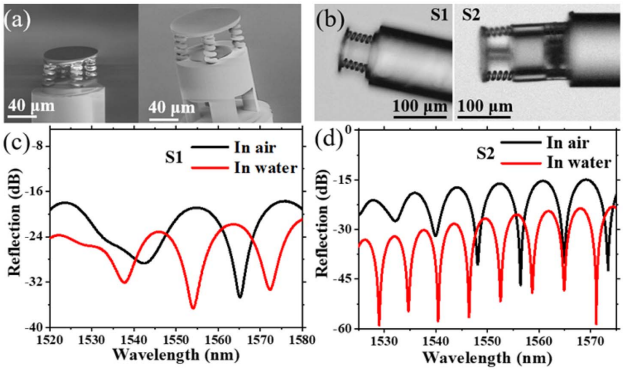

Fig. 4. Results of the 3D-printed devices. (a) Scanning electron images and (b) microscopic images of the fabricated microresonators. (c) and (d) Reflection spectra of the devices in atmospheric and aquatic environments.

and microscopic images of the devices with different cavity lengths. Figures 4(c) and 4(d) show the normalized reflected spectra of the devices in atmospheric and aquatic environments. It can be seen that the reflection in water decreases; however, the fringe contrast slightly increases. Sample 2 (S2) has a large fringe contrast of 30 dB, which is much higher than the reported 3D printed FP devices. Here, the FP device with a longer cavity shows the comparable reflections from the fiber tip and diaphragm, which leads to a high fringe contrast. Note that the sensitivity is related to this value. Therefore, for the following experiments, FPs with long cavities are used for acoustic wave sensing. Note that the supporting pillars can be vibrated, which can then change the device's resonant frequency. Therefore, the size of supporting pillar is designed to be large enough to avoid coupling.

To further investigate the fiber-tip-based, two-photon 3D fabrication, a few FP devices are fabricated. Since parameters such as the outer radius, wire radius, coil number, and pitch are used to tune the spring resonance behavior, different outer radii are chosen for fabrication of spring-tuning structures, as shown in Fig. 5. The top side of each figure in Fig. 5 shows the microscopic image of the fabricated device. The bottom sides of Figs. 5(a), 5(b), and 5(c) show the reflections of spring-tuning devices with different outer radii of 7 μm, 9 μm, and 11 μm, respectively, when the diaphragm thickness is 5 μm. Figures 5(d)–5(f) show the reflections of the devices with different outer radii when the diaphragm thickness is 1 μm. It can be seen that the devices immersed into water show additional loss. Due to the fabrication issues, some of the fringe contrasts are smaller. Here, the device with a highest fringe contrast [Fig. 5(b)] is used for acoustic wave sensing.

B. Ultrasound Detection

Based on the investigation of this FP cavity resonator, any stimulus on the plate will cause a vibration of the device and then lead to a change in phase. Here, the device is characterized for acoustic wave detection. To evaluate the response of the proposed FP microdevice, ultrasonic waves were generated using piezoelectric ultrasonic transducers driven by a function generator or pulser/receiver (DPR300, JSR Corp. Tokyo). The experimental setup is shown in Fig. 6, where a tunable laser (TUNICS T100S-HP, EXFO, Quebec City, Quebec, Canada) was used as the light source. The light transmitted through a circulator and was reflected by the device and detected by a photodetector connecting a digital oscilloscope. To characterize the input acoustic wave pressure, a commercial hydrophone [8104, Hottinger Brüel & Kjær A/S (HBK), Virum, Denmark] was used. All the driver and sensors were immersed into a water tank. To obtain a maximal sensitivity, the laser wavelength was locked at the quadrature point.

First, the low frequency response of the device was investigated, as shown in Fig. 7. In the measurements, the acoustic wave was generated by a broadband ultrasonic transducer (UT) with a central response frequency of 80 kHz. Figures 7(a) and 7(b) show the time and frequency responses of the fabricated device. The device had a peak frequency response at 83.9 kHz, which is very close to the simulation. To further investigate the noise equivalent acoustic signal level, a sinusoidal burst signal was generated, as shown in Fig. 7(c), where the amplitude was about 82.5 Pa and the frequency was 75 kHz. The inset of Fig. 7(c) shows the detected time response, and the frequency response shows a high SNR of 56.2 dB, which converts a noise equivalent acoustic signal level of 2.39 $mPa/Hz^{1/2}$.

Next, we investigated the high-frequency response of the device to sinusoidal acoustic waves with a frequency of 750 kHz by driving the UT with a burst sinusoidal electric

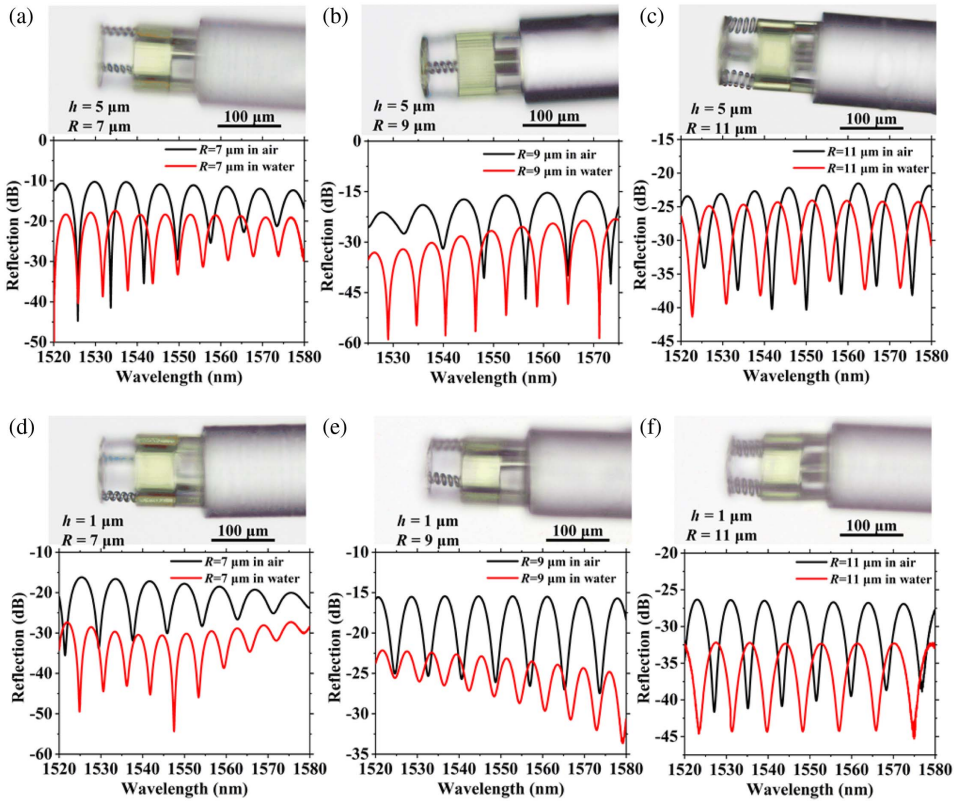

Fig. 5. Reflection spectra of the devices in atmospheric and aquatic environments. (a)–(c) Devices with a diaphragm thickness of 5 μm and an outer radius of (a) 7 μm, (b) 9 μm, and (c) 11 μm. (d)–(f) Devices with a diaphragm thickness of 1 μm and an outer radius of (d) 7 μm, (e) 9 μm, and (f) 11 μm.

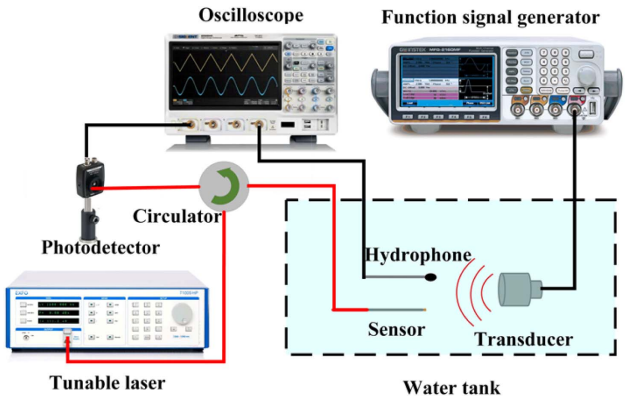

Fig. 6. Schematic diagram of the experimental setup for acoustic wave detection.

signal. High frequency modes near 800 kHz were obtained, as shown in Fig. 8(a), which is very close to the simulated results. Next, the sensitivity of acoustic wave pressure was characterized, as shown in Fig. 8(b). A continuous sinusoidal wave with a frequency of 750 kHz was generated. The detected signals with different input voltages were obtained, as shown in the inset of Fig. 8(b). It can be seen that the detected output varies linearly with the amplitude of the input signal. The slope is calculated as 0.0883 mV/V_{pp}, which converts into a displacement sensitivity of 22.4 nm/kPa. Additionally, the angle response of the device also was investigated. Just like the sensitivity experiment, a continuous sinusoidal wave with a frequency of 750 kHz was generated. The calculated amplitude of the detected signals versus the testing angle is shown in Fig. 8(c), where the inset shows the testing setup. It can be seen that device has relatively broad angular response, making the FP-based microresonator an ideal directional point detector for imaging applications.

C. Ultrasound Imaging

Optical fiber-based ultrasound imaging has received considerable attention in the last decades [28–30]. As well as high sensitivity, typically a well-behaved frequency response is important, which is sufficiently broadband to capture all relevant frequencies in an acoustic pulse signal. However, for microresonators, the resonating frequency is usually used as the sensitivity because the frequency is much higher. Here, we pick a nonresonant frequency as the sound source for data analysis. To demonstrate the practical applicability of ultrasound imaging, the fabricated device was used for underwater positioning and imaging, as shown in Fig. 9.

Figure 9(a) shows the schematic of the acoustic wave position and imaging measurement setup using the FP microresonator. The acoustic signal was generated by a water immersion UT (Olympus C306, 2.25 MHz central frequency, Evident Corp., Tokyo) connecting a pulser (DPR300, 35 MHz

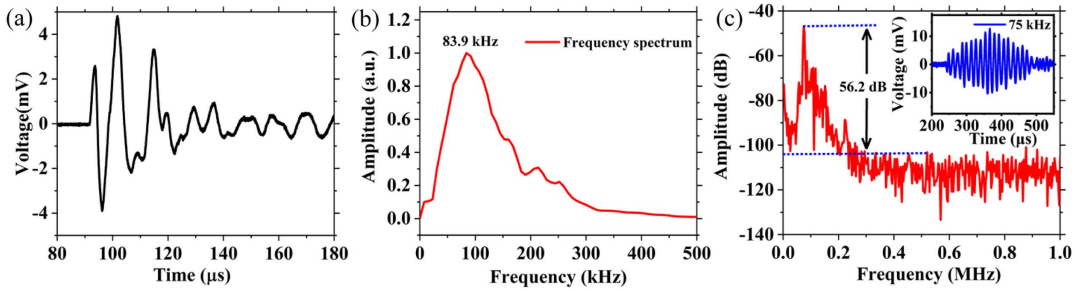

Fig. 7. Low frequency response of the device: (a) time response and (b) frequency response. (c) Acoustic response of the device to the sinusoidal burst signal with an amplitude of 82.5 Pa and a frequency of 75 kHz. The inset shows the detected time response.

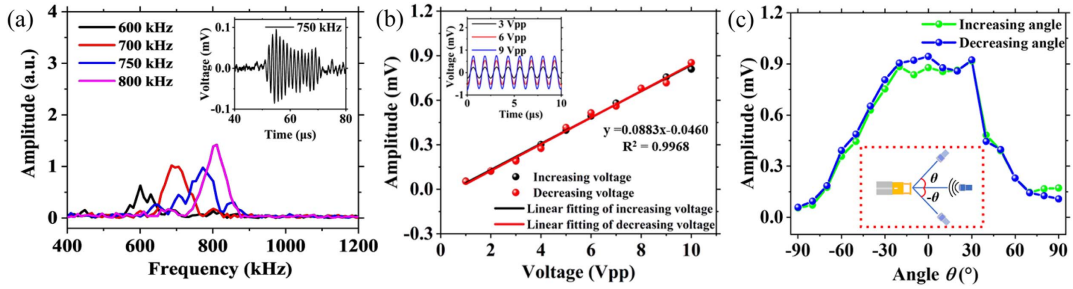

Fig. 8. (a) High acoustic response of the device to the sinusoidal burst signal. The inset shows a detected time signal at 750 kHz. (b) Acoustic wave pressure sensitivity and (c) angle response of the device.

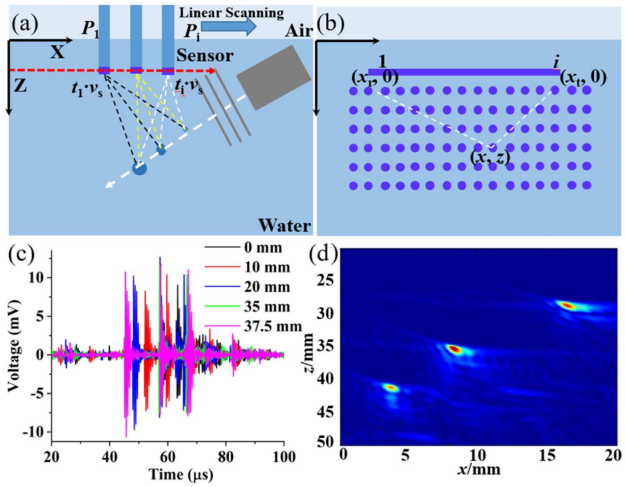

Fig. 9. (a) Schematic of the experimental setup. (b) Total focusing algorithm. (c) Detected signals at different detecting positions. (d) Reconstructed cross-section image of the objects.

bandwidth, JSR). Three steel pillars with a distance of a few millimeters were mounted under water. To realize the object positioning, the proposed FP acoustic device was used as a moving detector based on an ultrasonic total focusing method [31–33]. In this work, the UT was fixed at a position with a certain angle. The generated acoustic signal was reflected by the objects and detected by the fiber tip FP device, which was immersed into water and linearly scanned. Figure 9(b) illustrates the algorithm for the target positioning and imaging. The reflected information can be obtained at each specific phase based on this algorithm. Figure 9(c) shows a series of raw detected signals with no time averaging. It is clear that the reflected signal contains three strong peaks. According to the total focusing algorithm, the three targets with millimeter scale can be detected and the reconstructed cross-section image, as shown in Fig. 9(d), agrees well with the value set in the experiment. This demonstrates that the proposed fiber tip device can be used for high-resolution objective positioning and imaging.

4. CONCLUSION

In this work, we proposed what we believe, to the best of our knowledge, is a novel spring-based FP cavity microresonator, designed, fabricated, and used for acoustic wave detection and imaging. Two vibration modes of the resonator were observed. We found that the vibration modes can be coupled and optimized by changing the structure size. Compared to other reported micro-optomechanical FP cavities, the spring-based FP resonator exhibits a high ultrasound sensitivity, which can be used for underwater object imaging. It demonstrates that the proposed work has great potential in acoustic detection and biomedical imaging applications. To obtain a higher sensitivity, the optical performance of the device can be further improved by optimizing the fabrication issues. For high-resolution imaging, a sensor array can be designed in the future.

Funding. National Natural Science Foundation of China (62005153, 12174245); Natural Science Foundation of

Shanghai (20ZR1420300); National Key Research and Development Program of China (2022YFF0708400).

Disclosures. The authors declare no conflicts of interest.

Data Availability. Data underlying the results presented in this paper are not publicly available at this time but may be obtained from the authors upon reasonable request.

REFERENCES

1. R. Shnaiderman, G. Wissmeyer, M. Seeger, D. Soliman, H. Estrada, D. Razansky, A. Rosenthal, and V. Ntziachristos, "Fiber interferometer for hybrid optical and optoacoustic intravital microscopy," Optica **4**, 1180–1187 (2017).
2. H. Wei and S. Krishnaswamy, "Polymer micro-ring resonator integrated with a fiber ring laser for ultrasound detection," Opt. Lett. **42**, 2655–2658 (2017).
3. S. Basiri-Esfahani, A. Armin, S. Forstner, and W. Bowen, "Precision ultrasound sensing on a chip," Nat. Commun. **10**, 132 (2019).
4. H. Wei, C. Tao, Y. Zhu, and S. Krishnaswamy, "Fiber Bragg grating dynamic strain sensor using an adaptive reflective semiconductor optical amplifier source," Appl. Opt. **55**, 2752–2759 (2016).
5. Y. Liang, L. Jin, L. Wang, X. Bai, L. Cheng, and B. Guan, "Fiber-laser-based ultrasound sensor for photoacoustic imaging," Sci. Rep. **7**, 40849 (2017).
6. J. Ma, Y. He, X. Bai, L. Sun, K. Chen, K. Oh, and B. Guan, "Flexible microbubble-based Fabry–Pérot cavity for sensitive ultrasound detection and wide-view photoacoustic imaging," Photon. Res. **8**, 1558–1565 (2020).
7. H. Wei and S. Krishnaswamy, "Adaptive fiber-ring lasers based on an optical fiber Fabry–Perot cavity for high-frequency dynamic strain sensing," Appl. Opt. **59**, 530–535 (2020).
8. H. Fan, L. Zhang, S. Gao, L. Chen, and X. Bao, "Ultrasound sensing based on an in-fiber dual-cavity Fabry–Perot interferometer," Opt. Lett. **44**, 3606–3609 (2019).
9. W. Duque, C. Díaz, A. Leal-Junior, and A. Frizera, "Fiber-optic hydrophone based on Michelson's interferometer with active stabilization for liquid volume measurement," Sensors **22**, 4404 (2022).
10. C. Sun, "Multiplexing of fiber-optic acoustic sensors in a Michelson interferometer configuration," Opt. Lett. **28**, 1001–1003 (2003).
11. W. Zhu, D. Li, J. Liu, and R. Wang, "Membrane-free acoustic sensing based on an optical fiber Mach–Zehnder interferometer," Appl. Opt. **59**, 1775–1779 (2020).
12. L. Sun, T. Huang, Z. Yuan, W. Lin, P. Xiao, M. Yang, J. Ma, Y. Ran, L. Jin, J. Li, and B. Guan, "Ultra-high sensitivity of dual dispersion turning point taper-based Mach-Zehnder interferometer," Opt. Express **27**, 23103–23111 (2019).
13. P. Fomitchov, S. Krishnaswamy, and J. Achenbach, "Extrinsic and intrinsic fiberoptic Sagnac ultrasound sensors," Opt. Eng. **39**, 1972–1984 (2000).
14. W. Zhao, F. Wang, J. Wang, J. Li, Z. Huang, M. Zhang, Z. Wang, and Z. Cai, "A Sagnac-based interferometer with optimal polarization control for Lamb wave detection," Opt. Laser Technol. **143**, 107325 (2021).
15. W. Zhang, R. Wang, Q. Rong, X. Qiao, T. Guo, Z. Shao, J. Li, and W. Ma, "An optical fiber Fabry–Perot interferometric sensor based on functionalized diaphragm for ultrasound detection and imaging," IEEE Photon. J. **9**, 7103208 (2017).
16. Y. Sun, Z. Dong, Z. Ding, N. Wang, L. Sun, H. Wei, and G. P. Wang, "Carbon nanocoils and polyvinyl alcohol composite films for fiber-optic Fabry–Perot acoustic sensors," Coatings **12**, 1599 (2022).
17. Y. Wu, C. Yu, F. Yu, C. Li, J. Zhou, Y. Gong, Y. Rao, and Y. Chen, "A highly sensitive fiber-optic microphone based on graphene oxide membrane," J. Lightwave Technol. **35**, 4344–4349 (2017).
18. F. Yu, Q. Liu, X. Gan, M. Hu, T. Zhang, C. Li, F. Kang, M. Terrones, and R. Lv, "Ultrasensitive pressure detection of few-layer MoS_2," Adv. Mater. **29**, 1603266 (2017).
19. W. Ni, P. Lu, X. Fu, W. Zhang, P. P. Shum, H. Sun, C. Yang, D. Liu, and J. Zhang, "Ultrathin graphene diaphragm-based extrinsic Fabry-Perot interferometer for ultra-wideband fiber optic acoustic sensing," Opt. Express **26**, 20758–20767 (2018).
20. H. Wang, Z. Xie, M. Zhang, H. Cui, J. He, S. Feng, X. Wang, W. Sun, J. Ye, P. Han, and Y. Zhang, "A miniaturized optical fiber microphone with concentric nanorings grating and microsprings structured diaphragm," Opt. Laser Technol. **78**, 110–115 (2016).
21. X. Lu, Y. Wu, Y. Gong, and Y. Rao, "A miniature fiber-optic microphone based on an annular corrugated MEMS diaphragm," J. Lightwave Technol. **36**, 5224–5229 (2018).
22. B. Liu, H. Zhou, L. Liu, X. Wang, M. Shan, P. Jin, and Z. Zhong, "An optical fiber Fabry-Perot microphone based on corrugated silver diaphragm," IEEE Trans. Instrum. Meas. **67**, 1994–2000 (2018).
23. M. Yao, Y. Zhang, X. Ouyang, A. P. Zhang, H. Y. Tam, and P. A. Wai, "Ultracompact optical fiber acoustic sensors based on a fiber-top spirally-suspended optomechanical microresonator," Opt. Lett. **45**, 3516–3519 (2020).
24. J. A. Martins, D. Leite, and E. C. Romao, "Studying resonant frequencies of a helical spring with and without axial loads," J. Fail. Anal. Prev. **20**, 1301–1307 (2020).
25. J. Ma, H. Xuan, H. L. Ho, W. Jin, Y. Yang, and S. Fan, "Fiber-optic Fabry–Pérot acoustic sensor with multiplayer graphene diaphragm," IEEE Photon. Technol. Lett. **25**, 932–935 (2013).
26. D. Zhang, H. Wei, H. Hu, and S. Krishnaswamy, "Highly sensitive magnetic field microsensor based on direct laser writing of fiber-tip optofluidic Fabry–Pérot cavity," APL Photon. **5**, 076112 (2020).
27. H. Wei, M. Chen, and S. Krishnaswamy, "Three-dimensional-printed Fabry–Perot interferometer on an optical fiber tip for a gas pressure sensor," Appl. Opt. **59**, 2173–2178 (2020).
28. W. Zhang, F. Chen, W. Ma, Q. Rong, X. Qiao, and R. Wang, "Ultrasonic imaging of seismic physical models using a fringe visibility enhanced fiber-optic Fabry-Perot interferometric sensor," Opt. Express **26**, 11025–11033 (2018).
29. Z. Zou, Z. Qin, Y. Li, and Q. Liu, "Study on a health monitoring and defect imaging technology of special equipment that is based on optical fiber ultrasonic sensing," Opt. Fiber Technol. **61**, 102393 (2021).
30. J. A. Guggenheim, J. Li, T. J. Allen, R. J. Colchester, S. Noimark, O. Ogunlade, I. P. Parkin, I. Papakonstantinou, A. E. Desjardins, E. Z. Zhang, and P. C. Beard, "Ultrasensitive plano-concave optical microresonators for ultrasound sensing," Nat. Photonics **11**, 714–719 (2017).
31. H. Zhang, L. Zeng, G. Fan, H. Zhang, Q. Zhu, and W. Zhu, "Instantaneous phase coherence imaging for near-field defects by ultrasonic phased array inspection," Sensors **20**, 775 (2020).
32. W. Ji, L. Liu, Z. Xing, D. Zhang, Y. Wang, L. Chen, Y. Chen, X. Sun, and Y. Du, "Total-focus ultrasonic imaging of defects in solids using a PZT piezoelectric micromachined ultrasonic transducer array," IEEE Trans. Ultrason. Ferroelectr. Freq. Control **68**, 1380–1386 (2021).
33. A. Kumar, "Phased array ultrasonic imaging using angle beam virtual source full matrix capture-total focusing method," NDT & E Int. **116**, 102324 (2020).